Nanoscale

PAPER

View Article Online
View Journal | View Issue

Cite this: *Nanoscale*, 2018, **10**, 5366

Graphene-coated polymer foams as tuneable impact sensors†

Conor S. Boland, *[a] Umar Khan,[b] Mathew Binions,[a] Sebastian Barwich,[a] John B. Boland,[a] Denis Weaire[a] and Jonathan N. Coleman *[a]

Received 12th December 2017,
Accepted 28th February 2018

DOI: 10.1039/c7nr09247d

rsc.li/nanoscale

The use of graphene-based nanocomposites as electromechanical sensors has been broadly explored in recent times with a number of papers describing porous, foam-like composites. However, there are no reported foam-based materials that are capable of large dynamic compressive load measurements and very few studies on composite impact sensing. In this work, we describe a simple method of infusing commercially-available foams with pristine graphene to form conductive composites, which we refer to as G-foam. Displaying a strain-dependent electrical response, G-foam was found to be a reasonably effective pressure sensing material. More interestingly, G-foam is a sensitive impact-sensing material. Through the addition of various amounts of polymer filler, the mechanical properties of the composites can be tuned leading to the controllable variation of the impact sensing range. We have developed a simple model which quantitatively explains all our impact sensing data.

Introduction

In recent years, graphene has received unparalleled attention in composite research, largely due to its superlative mechanical and electrical properties.[1–3] Due to its high strength and stiffness,[4] graphene has widely been viewed as an ideal filler for the reinforcement of polymer matrices. Furthermore, the combination of its excellent electrical conductivity and the fact that it is often used as high aspect ratio nanosheets means that the addition of relatively small amounts of graphene to polymers renders them electrically conductive.

One composite application which combines both electrical and mechanical effects is electromechanical sensing. Such sensors display resistances which scale with strain, ε, or pressure, P, as:

$$\Delta R/R_0 = G\varepsilon = SP$$

where $\Delta R/R_0$ is the fractional resistance change on deformation, and G and P are the strain and pressure gauge factors (sensitivities). In general, composites yield excellent strain and pressure sensors because their resistivity tends to change with mechanical deformation, resulting in high sensitivity.[5] Composite strain sensors have been fabricated from a number of nano-materials but mainly incorporating nanotubes[6,7] and graphene.[8–11] Elastomer-based composite sensors are particularly attractive as wearable sensors due to their very low stiffness which is important for reasons of comfort.[5] In principle, stiffness could be reduced even further by using very soft, polymer-based foams as the sensing material.

Indeed, a number of graphene oxide-based foams have been used for pressure sensing.[12] For example, soaking preformed polyurethane foams in graphene oxide (GO) dispersions was shown to give conductive composites that were pressure sensitive[13–15] and displayed pressure gauge factors as high as S = 0.26 kPa^{-1}.[15] An alternative method, used GO based foam structures coated in polymer[16–19] and gave pressure gauge factors as high as 0.6 kPa^{-1}.[18] Such structures were demonstrated in applications from pulse measurement[18] to EMF shielding.[17]

However, a subtle point is that foams can be too soft when it comes to pressure sensing. Composite pressure sensors tend to have a range of compressible strain over which they can operate effectively. Assuming an approximately linear stress–strain response, this sets a limit for the maximum pressure which can be sensed: $P_{max} = Y\varepsilon_{max}$, where Y is the compressive modulus and ε_{max} is the maximum compressive strain for effective sensing. The GO-based foam composites reported in the literature tend to have relatively low modulus and so relatively small dynamic sensing ranges. To the authors knowledge, the largest pressure measured for composite foam sensors is 900 kPa.[18]

Similar arguments can be applied to composite impact sensors. Wearable impact sensors could be important in sports such as rugby, hurling or American football for monitoring the

[a]School of Physics, CRANN and AMBER Research Centres, Trinity College Dublin, Dublin 2, Ireland. E-mail: bolandc1@tcd.ie, colemaj@tcd.ie
[b]Institute of Technology Sligo, Ash Lane, Sligo, F91 YW50, Ireland

†Electronic supplementary information (ESI) available. See DOI: 10.1039/c7nr09247d

magnitude of impacts to the head or body. While composite impact sensors have been demonstrated, we are not aware of reports of foam-based impact sensors in the literature. Composite impact sensors convert kinetic energy of impact to compressive strain energy and output a resistance change which scales with the resultant compressive strain.[5] Equating the kinetic and compressive energies shows the maximum detectable kinetic energy to scale with sensor stiffness (for a maximum effective compressive strain). Again, this results in limited dynamic range for foam-based sensors.

Thus, there appears to be a gap in the literature which would benefit from the demonstration of foam-based composite pressure and impact sensors with controllable stiffness leading to a broad pressure detection range. In this work, we report on a method of infusing store bought foams with pristine graphene to form conductive composites which can sense compressive strain, pressure and impact. The stiffness, and so dynamic range, could be tuned by the addition of a polymer filler, resulting in a set of sensors which could detect impact energies from $\sim 10^{-4}$ to 3 J.

Results and discussion

Basic characterisation of G-foam

In this work, we fabricate electrically conducting composite foams by combining commercially available polymer foams with graphene nanosheets produced by liquid phase exfoliation. This nanosheet production method involves sonication or shearing of graphite powder in certain liquids such as solvents with appropriate surface energy as well as polymer or surfactant solutions.[20–25] Under optimised conditions, this procedure results in suspensions (concentration up to ~5 mg ml^{-1}) of largely defect-free few-layer graphene nanosheets with thickness of ~1–10 monolayers and lengths of ~100–1000 nm.[26,27] Such suspensions have been used to facilitate a wide range of applications, particularly in the area of functional composites.[28–36] Here, we exfoliate graphite powder by sonication in *N*-methyl-pyrrolidone (NMP) and redisperse in a water/surfactant solution resulting in few-layer nanosheets which are a few monolayers thick and have a mean length of 311 ± 8 nm (300 counts) (see Fig. 1A for example TEM image).

While composite formation generally involves mixing the filler with the polymer in either a solution or a molten environment,[5,37–40] here we take a different approach. By soaking pre-existing polymer foams in suspensions of graphene nanosheets, we infused the nanosheets into the porous internal volume of the foam. The nanosheets are then deposited onto the internal surface of the foam resulting in the formation of a nanosheet network coating.

To identify a suitable foam, we applied preliminary tests to a range of commercially available polymer foams (see ESI† and methods). We found that graphene could be infused into all foams tested, and in most cases a conductive composite was obtained (see Fig. S1†). However, we found that the composite conductivity tended to decrease significantly with increasing

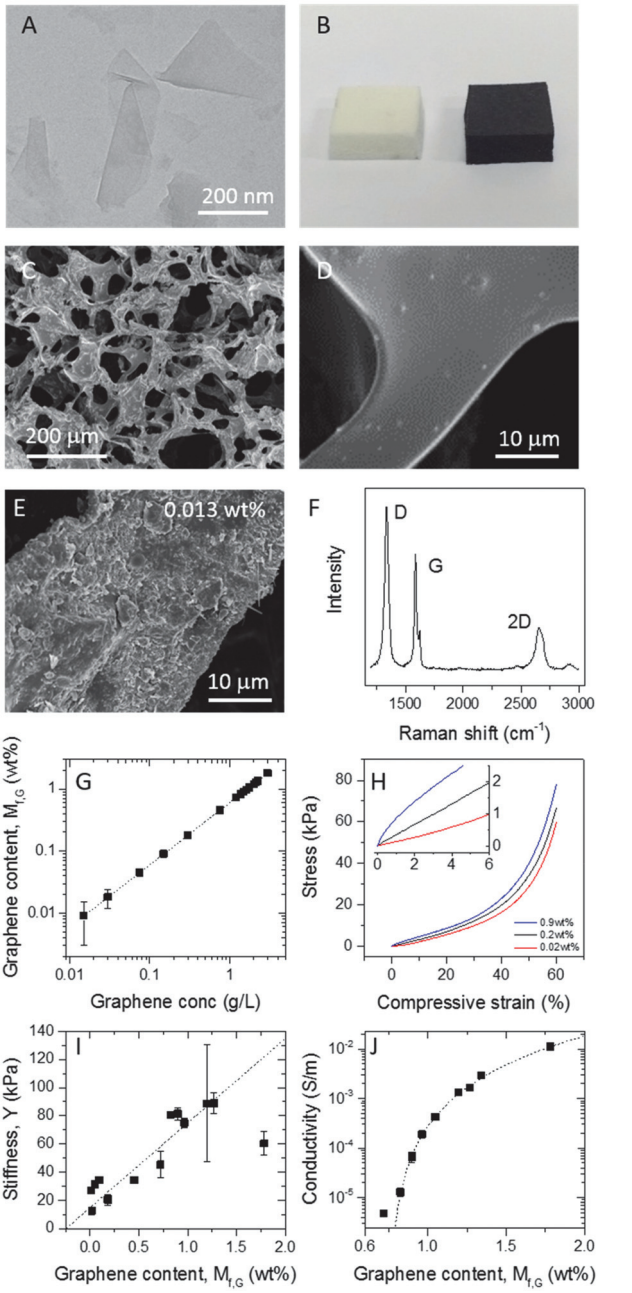

Fig. 1 Basic characterisation of graphene/foam composites. (A) Representative TEM image of liquid-exfoliated graphene nanosheets. (B) Photographs of untreated foam (left) and a graphene/foam composite (1 wt%). (C–E) SEM images showing the architecture of the starting foam and close-up images of the bare foam (D) and a graphene-coated foam composite (E). (F) Raman spectrum of a graphene/foam composite showing the characteristic D, G and 2D bands. (G) Graph showing the estimated graphene mass fraction in the final composite as a function of the graphene concentration in the soaking dispersion. (H) Compressive stress strain curves for composites with three representative loading levels. Inset: The low strain region. (I, J) Composite stiffness (I) and (zero-strain) conductivity (J) plotted as a function of graphene loading level. In (J), the line is a fit to eqn (4).

pore size. In addition, large-pore composite foams tended to give very weak or negative electromechanical response with non-trivial *G*- or *S*-values found only for the five foams with the smallest pore sizes. As a result of this optimisation process, we chose a small-pore polyurethane-based foam with a density of 280 kg m^{-3} (porosity = 87%) and a specific surface area of 0.42 m^2 g^{-1} (as measured by BET). This foam was used in all subsequent experiments and is shown on the left in Fig. 1B. SEM imaging (Fig. 1C and D) showed the foam to consist of a polymer network with struts a few tens of microns wide and pores in the size range ~50–200 μm. Though this particular foam was chosen as the optimum matrix for our sensing materials, we note that a number of the other foam materials might be optimised to produce a sensing material, especially those with small pore sizes.

The composites were formed by soaking the polymer foams (typically 2 cm × 2 cm × 6 mm) in graphene suspensions of different concentrations (0.015–3 mg ml^{-1}) for a fixed time (5 min). As described above, this resulted in significant take-up of graphene as evidenced by the blackening of the foam (Fig. 1B, right). SEM analysis showed the large-scale deposition of graphene nanosheets onto the internal surface area of the foam (Fig. 1E). The uptake of graphene can be confirmed by Raman spectroscopy on the foam which gave intense spectra dominated by the three main graphene Raman bands (Fig. 1F). We estimated the mass uptake (see Methods), which is plotted in Fig. 1G as graphene mass fraction ($M_{f,G} = M_{Gra}/(M_{Gra} + M_{poly})$) *versus* the concentration of graphene in the suspension in which the foam was soaked. We found we could controllably achieve mass fraction from ~2 wt% down to arbitrary low levels, allowing effective tuneability of graphene content.

However, we also found the resultant composites to be somewhat unstable, with the graphene coating appearing to detach over time. To address this we soaked all composites in a solution of polyurethane (PU) in water (5 mg ml^{-1}) for 5 min. This led to the infusion of PU into the foam and resulted in the formation of a PU coating, presumably on top of the graphene coating. Under these circumstances, we estimate the PU content within the composites at ~3 wt%. Such a coating resulted in an almost complete stabilisation of the composite with no evidence of graphene removal observed, even after repeated mechanical deformation. For simplicity, we refer to the resultant composites as G-foam.

We characterised the mechanical properties of G-foams with different graphene loading levels by compressive testing. Representative stress–strain curves for a subset of loading levels are shown in Fig. 1H. As might be expected the graphene coating had very little effect on the stress–strain curves as a whole. However, perhaps surprisingly, addition of graphene resulted in significant changes to the low strain portion of the curves (Fig. 1H inset). We characterise this by plotting the compressive stiffness of the G-foams as a function of graphene content (Fig. 1I), finding an approximately linear increase consistent with $dY/dM_{f,G}$ = 6 MPa. We interpret this by modelling the G-foam as two springs in parallel, one representing the polymeric foam and PU coating and one representing the graphene-network coating. Because parallel stresses can be added, this results in a rule-of-mixtures-like expression for compressive stress at a given strain:

$$\sigma_{G\text{-foam}} \approx \sigma_{G\text{-Net}} M_{f,G} + \sigma_{poly} \quad (1)$$

where σ_{Gra} and σ_{poly} are the stresses in the graphene coating and polymer respectively. The data in Fig. 1H would imply that at high strain, the polymeric stress dominates while at low strain the stress associated with the graphene network dominates. This difference suggests that while the polymer itself displays a superlinear stress strain curve, the stress in the graphene coating increases linearly (or sublinearly) with strain. In any case, by considering only low strains, we can divide eqn (1) by strain to give:

$$Y \approx Y_{G\text{-Net}} M_{f,G} + Y_{poly} \quad (2)$$

where Y, $Y_{G\text{-Net}}$ and Y_{poly} are the compressive stiffnesses of the composite, the graphene network and the polymer foam respectively. Fitting the data in Fig. 1I to eqn (2) would imply values of $Y_{G\text{-Net}}$ = 6 MPa and Y_{poly} = 15 kPa. We note that former value is small compared to tensile stiffnesses measured for thick vacuum filtered graphene nanosheet films (~5 GPa).[41] A significant portion of this difference may be explained by the differences in network geometry between these systems.

We also measured the in-plane electrical conductivity of G-foam as a function of graphene mass fraction as shown in Fig. 1J. We found the conductivity to be immeasurably low for mass fractions below 0.7 wt%. However, above this value we found a rapid increase in conductivity from $<10^{-5}$ S m^{-1} at 0.7 wt% to ~10^{-2} S m^{-1} at ~1.8 wt% graphene.

We interpret this behaviour as follows. Increasing the graphene mass fraction in these composites involves increasing the thickness of the graphene coating on the internal surface of the foam. For thin coatings of graphene nanosheets, it is known that the film conductivity, σ_e, is described by percolation theory:

$$\sigma_e \propto (t - t_c)^n \quad (3)$$

where t is the effective thickness of the graphene nanosheet coating and t_c and n are the percolation threshold and exponent respectively.[42,43] The percolation threshold can be thought of as the effective coating thickness where the first conducting path of nanosheets occurs. The effective coating thickness is just the thickness of a continuous film of the same density of the nanosheet network (ρ_{net}). This allows us to relate the areal mass density [kg m^{-2}] associated with the graphene coating, M_G/A, to the effective thickness using $M_G/A = \rho_{net} t$. Then, relating the graphene mass fraction to the areal mass density *via* the specific internal surface [m^2 kg^{-1}], A/M_T ($M_{f,G} = (M_G/A)(A/M_T)$), allows us to write $t = M_{f,G}/\rho_{net} \times (A/M_T)$ and so,

$$\sigma_e \propto (M_{f,G} - M_{f,G,c})^n \quad (4)$$

This expression fits the data in Fig. 1J very well with a critical loading level (percolation threshold) of $M_{f,G,c}$ = 0.75 wt%

and n = 2.6. Similarly, in a graphene oxide (GO)/polyvinylidene fluoride (PVDF) foam composite a percolation threshold of $M_{f,G,c}$ = 0.5 wt% and exponent of n = 2.66 were observed.[17] Using the relation given above we can convert $M_{f,G,c}$ into the nanosheet coating thickness at the percolation threshold (taking A/M_T = 0.42 m^2 g^{-1} and ρ_{net} ~1000 kg m^{-2}, a typically observed value), finding t_c ~20 nm.

Electromechanical properties of G-foam

Because the low-strain mechanical properties and the electrical properties of the G-foam are both controlled by the presence of the nanosheet network, it is likely that these properties are coupled. To test this, we performed experiments where we compressed the foam vertically while monitoring strain, stress (pressure) and electrical resistance (out-of-plane). In these experiments, the resistance was measured along the same direction as the deformation. Shown in Fig. 2A and B are plots of fractional resistance change *versus* strain (A) and pressure (B) for three typical graphene loading levels. In each case, we see an increase in resistance at low strain/pressure followed by a resistance decrease at higher strain/pressure. The resistance decrease at high strain/pressure is not interesting as it just reflects geometrical changes under deformation (as the material is compressed the inter-electrode separation decreases resulting in a resistance drop). However, the fact that the resistance falls at higher strain means that such materials can only be used as low-strain sensors (max strain 10–30% depending on graphene content). Much more interesting is the initial resistance increase which can be used to sense small strains or pressures. Such changes are associated with mechanically-induced changes in the resistivity of the G-foam (*i.e.* those changes not associated with sample dimensional changes). Such resistivity changes are generally considered to be due to changes in inter-nanosheet tunnelling resistances associated with changes in inter-nanosheet distances under strain. However, it should be noted that a recent publication has suggested that the resistivity change under strain can be more effectively described by considering strain-induced changes in nanosheet network connectivity.[5]

In either case, we can characterise the magnitude of the resistance change by the gauge factor which can be defined for strain (ε) or pressure (P) sensors as $G = \mathrm{d}(\Delta R/R_0)/\mathrm{d}\varepsilon|_{\varepsilon\to 0}$ or $S = \mathrm{d}(\Delta R/R_0)/\mathrm{d}P|_{P\to 0}$ respectively. We have calculated both strain and pressure gauge factors for all composites which are plotted *versus* graphene content in Fig. 2C and D. In each case, we see a clear peak in sensitivity which occurs very close to the electrical percolation threshold (0.75 wt%). As is often the case, the peak sensitivities were found just above the percolation threshold to be G = 4 and S = 0.05 kPa^{-1}. In comparison to literature, both values are rather low when looking at other pressure-sensing foam materials (see ESI†). Above the percolation threshold, the sensitivities fall off, apparently exponentially with a decay constant of 0.32 wt%. In practice, this suggests the graphene content should be as close to the percolation threshold as possible. However, it should be pointed out that as the percolation threshold is approached from above, the G-foam conductivity falls rapidly (eqn (4)) resulting in high operating resistances. Thus, practical sensors will require an optimisation of graphene content to give high values of G while maintaining reasonable sample resistances.

Repeatability and cycleability are important for any practical sensing material. To test this, we exposed the G-foam to a near

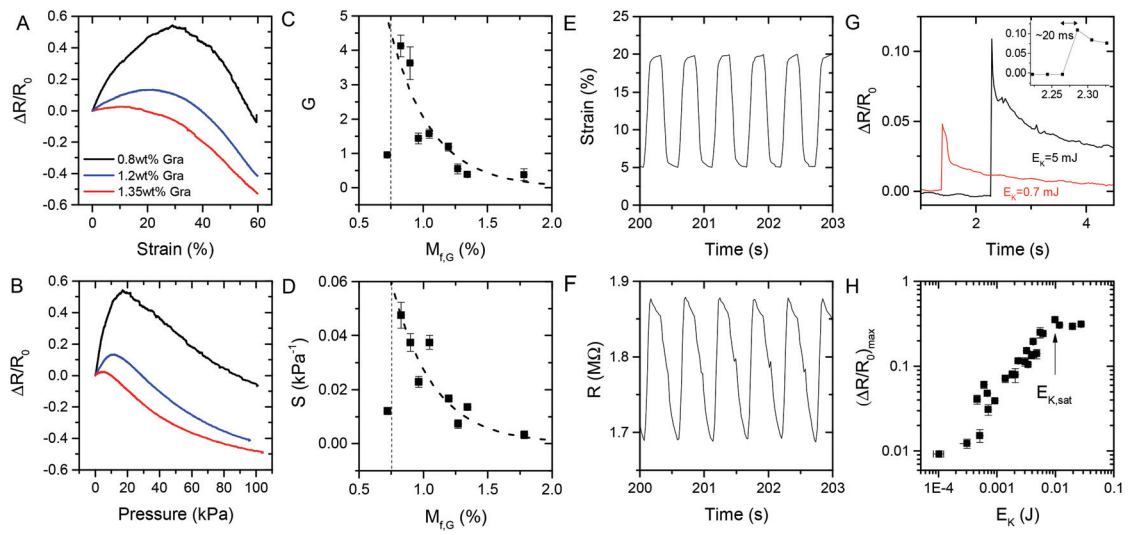

Fig. 2 Electromechanical properties of graphene foam. (A, B) Fractional resistance change as a function of both compressive strain (A) and pressure (B) with associated sensitivities, G and S, shown in (C) and (D) respectively. In (C) and (D) the vertical lines represent the percolation threshold while the dotted lines represent (empirically observed) exponential decays of sensitivity with graphene content. (E, F) Cyclic response of the graphene/foam composite (0.8 wt%) to a near-harmonic strain (E) with the resistance response shown in (F). (G) Temporal response of graphene/foam composite (0.8 wt%) resistance to an impact. (H) Maximum resistance change as a function of kinetic energy associated with impact. N.B. All the foams described in Fig. 2 contain 3 wt% PU to stabilise the graphene coating.

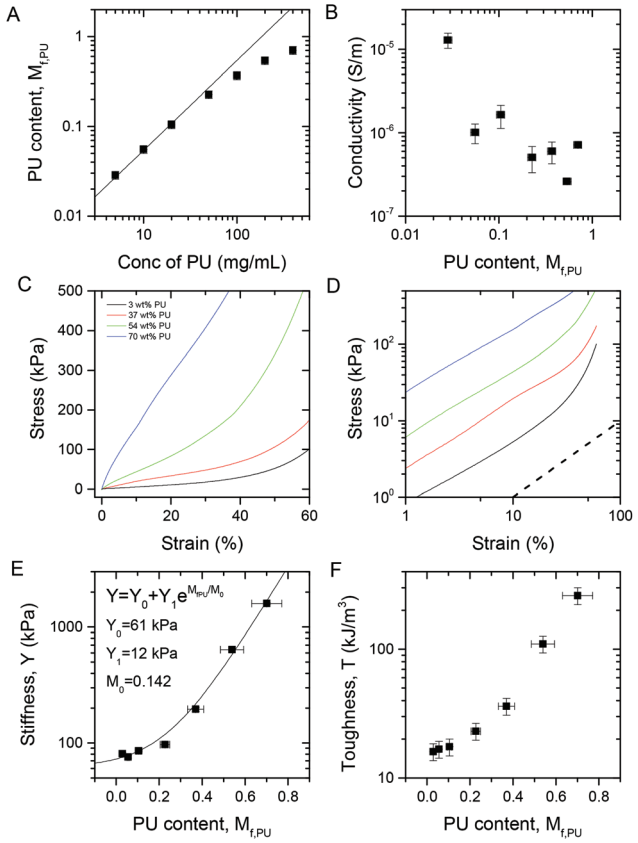

Fig. 3 Addition of polyurethane (PU) to graphene-foam composites (0.8 wt% graphene) to tune the electromechanical properties. (A) Estimated mass fraction of infused polyurethane in the final composites as a function of concentration of PU soaking solution. (B) Conductivity of graphene/foam composite as a function of infused PU mass fraction. (C, D) Stress strain curves for a range of infused PU mass fractions. N.B. the main panel shows a lin-lin plot while log–log plots are shown in D. The dashed line in D represents linearity. (E, F) Stiffness (E) and toughness (F) of graphene/foam composites as a function of infused PU mass fraction. In E the solid lines shows an empirical fit showing an exponential-like increase. In F the toughness represents the average area under the stress strain curves, integrated up to a compressive strain of 60%.

harmonic compressive strain cycle with period of 1 s and minimum and maximum strains of 5 and 20% (Fig. 3E). We found a resistance response (Fig. 2F) which was extremely repeatable over at least 400 cycles. While the resistance waveform wasn't perfectly harmonic, we attribute this to non-linearities in the resistance-strain curve (Fig. 2A), especially over the large strain range applied here.

It is clear from the data above those G-foam acts as a reasonable strain- and pressure sensor. However, the pressure sensing sensitivities, S, are rather low compared to composite foam pressure sensors described in the literature (typical values range from 0.1 to 2 kPa^{-1}, see ESI†). Nevertheless, as mentioned above, one electromechanical sensing application that is not often explored, but might be particularly suited to G-foams, is the sensing of impact. Such a sensor should output information related to either the average force or energy associated with the impact as well as the impact time. To test if this can be achieved with G-form, we built a test rig based on a mass on the end of a hinged arm, which could be controllably dropped on the G-foam. Then, we measure the magnitude of the impact *via* the kinetic energy (E_K) which we set equal to the initial gravitational potential energy of the mass, $E_K = mgh$, where m is the mass and h is the initial height. We note that, in these experiments, the initial and final resistances are not expected to be identical as the mass remains on top of the foam and thus compressing it after impact.

We measure the G-foam out-of-plane resistance as a function of time over the course of the impact. Two typical resistance waveforms are shown in Fig. 2G and consist of sharp resistance increases, which coincides with the impact, followed by a slow resistance decay as the foam settles down after the impact. The inset shows the region of impact and implies an impact time of <20 ms. The initial rapid increase in resistance is clearly a measure of the impact magnitude. We note that recent experiments on a graphene-filled polysilicone sensor (G-putty) showed the impact response to be related to impact energy rather than force or impulse.[5] We will demonstrate a simple model below which leads to the same conclusion for G-foam. We performed a number of impact tests, dropping different masses from a range of heights. Shown in Fig. 2H is a plot of the maximum resistance change, $(\Delta R/R_0)_{max}$, *versus* the impact energy, E_K. We found $(\Delta R/R_0)_{max}$ to increase with E_K in a well-defined way up to $E_{K,sat}$ = 0.01 J, after which the response saturated at $(\Delta R/R_0)_{max}$ ~0.35. The increase in $(\Delta R/R_0)_{max}$ at low impact energy is due to the effects of network deformation and has the same origins as the strain and pressure sensing described earlier. However, the saturation is clearly associated with the maximal compression of the foam such that the porosity approaches zero and further modification of the graphene network is impossible. That this saturation occurs at relatively low impact energy is due to the soft nature of the foam. This is a significant problem as it means impact energies above 0.01 J cannot be quantitatively measured. In fact, this value is relatively low and is consistent with a 10 g object falling a distance of 10 cm. Practical impact sensing will require the ability to detect much larger impacts than this.

Stiffening by polymer infiltration

The maximum resistance change saturates at high impact energies because the foam becomes fully compressed under these circumstances. One strategy to avoid such full compression would be to increase the energy absorbed by the foam during compression, leading to lower compressive strains for a given impact energy. This requires increasing the compressive toughness which is simply the absorbed energy density at a given compressive strain (ε') and is given by $T(\varepsilon') = \int_0^{\varepsilon'} \sigma d\varepsilon$. Clearly, the simplest way to increase this parameter is to increase the stress required to compress the foam to a given strain *i.e.* increase the stiffness.

We achieved this by increasing the amount of PU which was infused into the foam to mechanically stabilise the graphene coating. Instead of soaking the graphene-infused foams in a PU solution of concentration 5 mg ml^{-1} for 5 minutes, we soaked foams (0.8 wt% graphene before soaking) in a range of PU solutions with concentrations ranging from 10 to 400 mg ml^{-1} for 5 minutes with the expectation that higher PU concentrations would lead to higher degrees of PU infiltration and adsorption onto the internal surface area. After drying, the resultant PU content was estimated by comparing weight before and after soaking and is plotted as a mass fraction *versus* PU concentration in Fig. 3A. A well-defined trend is seen with PU contents growing from ~3 wt% to ~75 wt% as the PU concentration was increased from its original level of 5 mg ml^{-1} to 400 mg ml^{-1}.

The conductivity of the PU-treated foam fell by up to two orders of magnitude as the PU content was increased (Fig. 3A). This indicates that, as the PU adsorbs onto the infused graphene layer, it somehow disrupts the network connectivity resulting in a drop in conductivity. However, the mechanical properties improved significantly with increasing PU content (Fig. 3C and D). Additionally, the stress strain curves became much more linear over most of the strain range as more PU was added (Fig. 3D). Interestingly, the stiffness increased exponentially with PU content: very little change in stiffness was observed below ~25 wt% PU although a rapid stiffening by over an order of magnitude was observed for PU levels above this value (Fig. 3E). Likewise, the compressive toughness (defined here as the energy absorbed up to a strain of 60%, divided by the initial sample volume) increased relatively slowly up to an infused PU content of 20% before increasing more rapidly thereafter. The toughness of the foams with the highest PU loading levels were more than 10 times higher than the initial G-foam. This is important as this increased energy absorption capability should reduce the problem of resistance saturation under high impacts described above.

We also measured the electromechanical response of the PU-treated G-foams (Fig. 4A and D). As before, the resistance first increases and then decreases as either strain (Fig. 4A) or pressure (Fig. 4C) is increased. The peak in resistance determines the maximum compressive strain and maximum pressure (P_{max}) detectable using these sensors. As expected P_{max} increases steadily as the stiffness and toughness of the foam increases (Fig. 4C inset). Interestingly both strain-sensitivity (G) and pressure sensitivity (S) decrease exponentially as the infused PU content rises. While the exact nature of this decrease remains unknown, it may be related to the disruption of the graphene network posited above. However, it is worth noting, that even with reduced sensitivity, the PU infused graphene is a reliable sensor with a very reproducible electrical response to a near harmonic compressive strain (Fig. 4E and F). Interestingly, the gauge factor, G, does not exhibit significant rate dependence for any PU content (Fig. S2†).

Tuneable impact sensing

Given that the infusion of PU into the G-foams had somewhat increased their toughness, it is likely that the saturation impact energy might be shifted to higher values relative to the original G-foam. To explore this, we performed impact tests with a range of impact energies on a number of PU-infused G-foams with different PU contents. Two examples of impact response curves are shown in Fig. 5A and B. In both cases, a sharp increase in resistance is observed in impact followed by a gradual decline. We note that the resistance does not return to its original value as, in our apparatus, the dropped mass remains on the sample, forcing it to remain compressed after

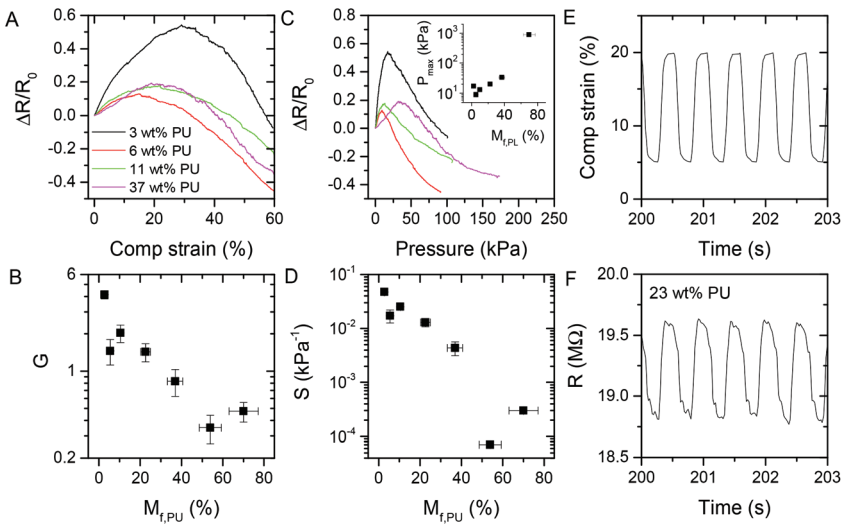

Fig. 4 Electromechanical properties of PU-infused graphene foam. (A–D) Fractional resistance change as a function of both compressive strain (A) with associated sensitivity, G, shown in (B) and pressure (C) with associated sensitivity, S, shown in (D). The inset in C represents the maximum pressure that can be practically detected, plotted *versus* PU mass farction. (E, F) Cyclic response of the PU-infused graphene/foam composite (23 wt%) to a near-harmonic strain (E) with the resistance shown in (F).

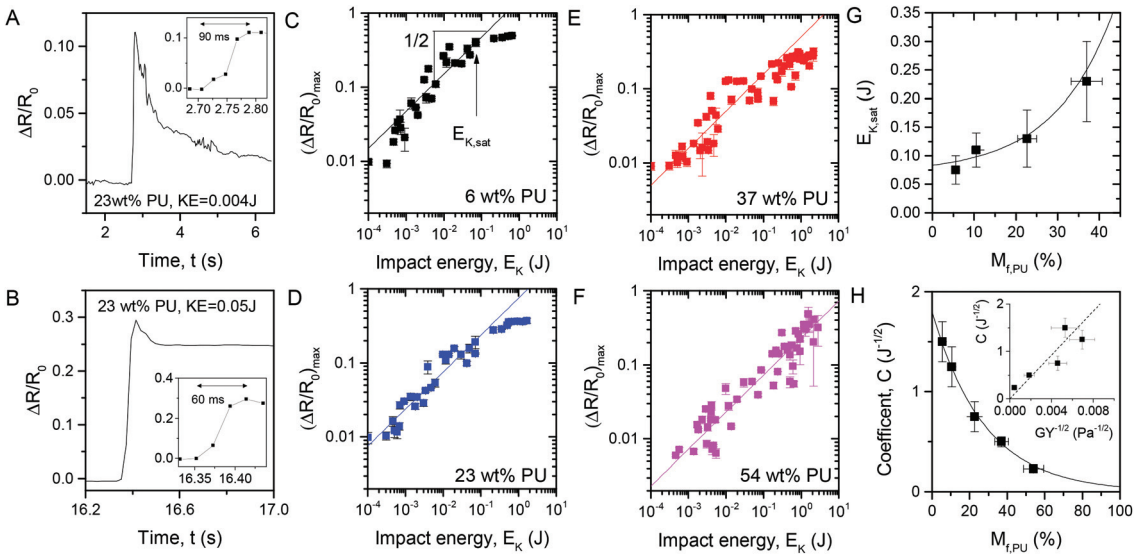

Fig. 5 Impact response of PU-infused graphene foam. (A, B) Temporal resistance responses of PU-infused graphene/foam composites to impacts associated with two potential energies. The insets display magnified views showing the rise time. (C–F) Maximum fractional resistance change on impact plotted *versus* potential energy of impact for composites with 4 different PU loading levels. The dashed lines are fits to $(\Delta R/R_0)_{max} = C \times E_K^{1/2}$. (G) Saturation potential energy (potential energy where the experimental data deviates from the fit line) plotted *versus* infused PU mass fraction. The line represents the semi-empirical model described in the text. (H) Coefficient, *C*, plotted *versus* infused PU mass fraction. Inset: Coefficient, *C*, plotted *versus* $G/\sqrt{Y}$, demonstrating he validity of eqn (8).

the test. Interestingly, as shown in the insets, the response time of the sensors containing additional PU was >60 ms, considerably longer than those with minimal PU (~20 ms).

Shown in Fig. 5C–F are data for the maximum fractional resistance change on impact plotted *versus* impact energy. There are two things of note in these graphs. Firstly, as the infused PU content is increased, the saturation of $(\Delta R/R_0)_{max}$ at high impact energy becomes less prominent and ultimately disappears by a PU content of 54%. We show this graphically by plotting the approximate value of impact energy where saturation begins, $K_{K,sat}$, *versus* infused PU content in Fig. 5G. This clearly shows the saturation onset to increase in energy as PU is added and the foam stiffens and toughens.

Secondly, the data in Fig. 5C–F seem to be roughly consistent with a square root relationship between $(\Delta R/R_0)_{max}$ and the impact energy, at least for midrange impact energies. We can understand this as follows. On impact, the kinetic energy of the falling mass is converted into elastic strain energy of the compressed foam. This can be quantified simply *via* the observation that as more PU was infused into the foam, its compressive stress–strain behaviour (Fig. 3C) became much less nonlinear compared to the original G-form (Fig. 1H) allowing us to make the crude approximation that $\sigma \approx Y\varepsilon$ over the whole strain range (σ is compressive stress, Y is the modulus and ε is compressive strain). This allows us to write

$$E_K \approx \frac{AL_0 Y \varepsilon_{max}^2}{2} \quad (5)$$

where the second term represents the potential energy associated with the compressed G-foam after the mass has come to rest. Here, A is the compressed area, L_0 is the initial foam thickness and ε_{max} is the final compressive strain. This allows us to write

$$\varepsilon_{max} \approx \sqrt{2 \times E_K / AL_0 Y} \quad (6)$$

Then, approximately relating the maximum resistance change to the maximum strain *via* $(\Delta R/R_0)_{max} \approx G\varepsilon_{max}$, gives:

$$(\Delta R/R_0)_{max} \approx G\sqrt{\frac{2 \times E_K}{AL_0 Y}} = C\sqrt{E_K} \quad (7)$$

where C can be thought of as the impact sensitivity parameter. Noting that $G = SY$ we can write C in terms of either G or S:

$$C = G\sqrt{\frac{2}{AL_0 Y}} = S\sqrt{\frac{2Y}{AL_0}} \quad (8)$$

This very simple model predicts the observed behaviour. The lines in Fig. 5C–F represents fits of eqn (7) to the data. We have extracted C from the fits and plotted it *versus* infused PU content in Fig. 5H. From this data, it is clear that the impact sensitivity parameter (C) falls off rapidly as the PU content is increased. Thus, removing the saturation problem comes at the cost of reduced sensitivity. However, this is not such a significant problem as it would only be necessary to address the problem of saturation when sensing large impacts where high sensitivity is not so crucial. In practical impact sensing devices, it would be possible to mount a high sensitivity sensor in series with a low sensitivity. Then for low impacts, only the high sensitivity (less stiff) device would be effected. However, for large impacts, the high sensitivity device would

be immediately fully compressed, allowing the low sensitivity (high stiffness) device to respond.

In addition, eqn (6) allows us to model $E_{K,sat}$ as the kinetic energy for which $\varepsilon_{max} \rightarrow 1$, giving $E_{K,sat} = AL_0Y/2$. Then, combining the empirical equation for $Y(M_{f,PU})$ given in Fig. 3E with the experimental initial foam volume ($AL_0 = 2.3 \times 10^{-6}$ m^2), gives an equation for $E_{K,sat}$ which fits the data in Fig. 5G extremely well, without the need for any adjustable parameters.

Eqn (8) predicts an approximate relationship between the impact sensitivity parameter (C) and the gauge factor (G). We can test this relationship by plotting C *versus* $G/\sqrt{Y}$ in Fig. 5H inset. We find a reasonably straight line, again supporting the validity of our model.

Conclusions

In conclusion, we have demonstrated a simple method to produce foam-based, polymer-graphene pressure and impact sensors. Although the as-produced sensors have a relatively low dynamic range (*i.e.* detectable pressure and impact energy range), this can be extended significantly by diffusing polymer into the interior of the foam to increase its stiffness. By developing a simple theory to describe the impact response of these sensors, we can outline a roadmap for improving sensor performance. Because impact sensitivity scales as $G/Y^{1/2}$ and dynamic range scales with Y, we need to develop foam-based sensor with significantly increased gauge factor (G) and moderately increased stiffness (Y). This might be achieved by a more sophisticated foam fabrication method. We believe these materials might find uses as low-cost pressure sensors or more probably as impact sensors for use in sports helmets or medical devices.

Methods

Graphene dispersions were prepared by the ultrasonic tip-sonication of graphite (Branwell, Graphite Grade RFL 99.5) in *N*-methyl-pyrrolidone (NMP) at 100 mg mL^{-1} (total volume ~300 mL) for 72 h at 80% amplitude. This was followed by a mild centrifugation at 1500 rpm for 90 min to remove unexfoliated aggregates and very large nanosheets. The removed supernatant was then vacuum filtered onto a 0.1 μm pore size polyester membrane to form a thick film of reaggregated nanosheets. This film was then redispersed at high concentration (~5 mg mL^{-1}) in water surfactant (sodium cholate; Sigma Aldrich) by ultrasonic tip-sonication for ~1.5 h to form a stock solution from which all composites were formed.

TEM grids were prepared by first diluting the dispersions and then drop-casting them onto holey carbon grids (Cu 400 mesh). Residual solvent was removed from the grids by drying in a vacuum oven. Bright field TEM images were obtained using a Jeol 2100 operating at 200 keV. Raman spectroscopy was performed on the graphene infused foams with a Horiba Jobin Yvon LabRAM HR800 with 633 nm excitation laser in air under ambient conditions. The Raman emission was collected by 100× objective lens (N.A. = 0.8) and dispersed by a 600 line per mm grating using 10% of the laser power (~2 mW). A total of 5 spectra were collected at different positions, baseline-corrected and averaged.

A series of preliminary electromechanical tests were performed on 11 store-bought foams which varied in pore size and density. Before infusion, all foams were cut into similar dimensions. The foams were then soaked in the same volume and concentration of graphene and PU dispersion. The sensing performance of the foams were found to be highly depended on the structure of the tested foams (see ESI†). A polyurethane (PU) based cosmetic face sponges purchased from Boots™ (Face – Soft Cosmetic Sponge; product #75-32-229) were chosen as the optimum foam for composite production based on its sensing performance. Foams for the preliminary and the preceding tests in this work were prepared in the following fashion. The foam was cut into 2 cm × 2 cm × 5.75 mm ($L \times W \times H$) pieces. After cutting to shape, the foam pieces were washed in deionised water three times before being dried in a vacuum oven for 5 h at 50 °C. The pre-washed foam pieces were then soaked in graphene dispersions diluted from the stock solution, with concentrations ranging from 0.015 mg mL^{-1} to 3 mg mL^{-1}. To insure complete infusion of the foam, the pieces were pre-compressed by hand before being adding to the dispersion. Foam pieces were soaked in a constant volume of graphene dispersion (4 mL) for 5 min and dried in a vacuum oven for 5 h at 50 °C. Graphene uptake was measured by recording the mass before and after soaking using an accurate balance.

To insure that the internal coating of graphene did not deteriorate during testing, the graphene infused foams were soaked in a 5 mg mL^{-1} PU/water dispersion (Michelman, product #U2022). Again, to insure complete infusion of the foam, the pieces were pre-compressed by hand before adding to the dispersion. Foam pieces were soaked in a constant volume of PU dispersion (3.8 mL) for 5 min and dried in a vacuum oven for 5 h at 50 °C to form the final composite. PU uptake was measured by recording the mass before and after soaking using an accurate balance. When looking at the effect of PU content on mechanical and electromechanical properties of the composites, PU soaking dispersion concentration was varied from 5 mg mL^{-1} to 400 mg mL^{-1} for a particular graphene content using the previously described methods above.

Scanning electron microscopy on the composites was undertaken using a Zeiss Ultra Plus. Using the SE2 detector, samples were examined at a working distance of ~2 mm, with a 30 μm aperture and a voltage of 5 kV. Compressive electromechanical measurements were performed using a Keithley KE2601 source meter in a 2-probe mode, controlled by LabView software, in conjunction with a Zwick Z0.5 ProLine Tensile Tester (100 N Load Cell). Contacts were painted on the test samples with silver paint, top and bottom of foam, with silver wires leads attached. The source meter was attached through the wire leads using crocodile clips. For the electro-

mechanical tests, the sample was place between two plates, with the bottom plate being stationary and the top plate applying the compressive force. Tests were performed at 2 mm min^{-1} until 60% applied strain.

Impact tests were performed initially by dropping bearings of varying masses (1–7 g) from a range of heights (1–9 cm). For larger weights, a hinged arm was constructed to controllably drop heavier weights (40 g–3 kg) from a similar range of heights. In both cases, the electrical response was measured with a sampling rate of 1 point per 0.01 s as a function of time.

Conflicts of interest

There are no conflicts to declare.

Acknowledgements

We acknowledge financial support from the SFI-funded AMBER research centre (SFI/12/RC/2278). JNC acknowledges funding from the European Union Seventh Framework Programme under grant agreement n°696656 Graphene Flagship. CS Boland is grateful for financial support through CRANN.

References

1 A. K. Geim, Graphene: Status and Prospects, *Science*, 2009, **324**(5934), 1530–1534.
2 A. K. Geim and K. S. Novoselov, The rise of graphene, *Nat. Mater.*, 2007, **6**(3), 183–191.
3 A. H. Castro Neto, F. Guinea, N. M. R. Peres, K. S. Novoselov and A. K. Geim, The electronic properties of graphene, *Rev. Mod. Phys.*, 2009, **81**(1), 109–162.
4 C. Lee, X. Wei, J. W. Kysar and J. Hone, Measurement of the Elastic Properties and Intrinsic Strength of Monolayer Graphene, *Science*, 2008, **321**(5887), 385–388.
5 C. S. Boland, U. Khan, G. Ryan, S. Barwich, R. Charifou, A. Harvey, C. Backes, Z. Li, M. S. Ferreira, M. E. Möbius, R. J. Young and J. N. Coleman, Sensitive electromechanical sensors using viscoelastic graphene-polymer nanocomposites, *Science*, 2016, **354**(6317), 1257.
6 P. Worajittiphon, M. J. Large, A. A. K. King, L. Jurewicz and A. B. Dalton, Stretchable conductive networks of carbon nanotubes using plasticized colloidal templates, *Front. Mater.*, 2015, **7**, 15.
7 J. C. Fernandez-Toribio, A. Iniguez-Rabago, J. Vila, C. Gonzalez, A. Ridruejo and J. J. Vilatela, A Composite Fabrication Sensor Based on Electrochemical Doping of Carbon Nanotube Yarns, *Adv. Funct. Mater.*, 2016, **26**(39), 7139–7147.
8 V. Eswaraiah, K. Balasubramaniam and S. Ramaprabhu, Functionalized graphene reinforced thermoplastic nanocomposites as strain sensors in structural health monitoring, *J. Mater. Chem.*, 2011, **21**(34), 12626–12628.
9 V. Eswaraiah, K. Balasubramaniam and S. Ramaprabhu, One-pot synthesis of conducting graphene–polymer composites and their strain sensing application, *Nanoscale*, 2012, **4**(4), 1258–1262.
10 L. Chen, G. H. Chen and L. Lu, Piezoresistive behavior study on finger-sensing silicone rubber/graphite nanosheet nanocomposites, *Adv. Funct. Mater.*, 2007, **17**(6), 898–904.
11 Y. S. Zhu, J. W. Li, H. B. Cai, Y. M. Wua, H. Y. Ding, N. Pan and X. P. Wang, Highly sensitive and skin-like pressure sensor based on asymmetric double-layered structures of reduced graphite oxide, *Sens. Actuators, B*, 2018, **255**, 1262–1267.
12 B. X. Zhang, Z. L. Hou, W. Yan, Q. L. Zhao and K. T. Zhan, Multi-dimensional flexible reduced graphene oxide/polymer sponges for multiple forms of strain sensors, *Carbon*, 2017, **125**, 199–206.
13 R. M. Hodlur and M. K. Rabinal, Self assembled graphene layers on polyurethane foam as a highly pressure sensitive conducting composite, *Compos. Sci. Technol.*, 2014, **90**, 160–165.
14 C. Wu, X. Huang, X. Wu, R. Qian and P. Jiang, Mechanically Flexible and Multifunctional Polymer-Based Graphene Foams for Elastic Conductors and Oil-Water Separators, *Adv. Mater.*, 2013, **25**(39), 5658–5662.
15 H.-B. Yao, J. Ge, C.-F. Wang, X. Wang, W. Hu, Z.-J. Zheng, Y. Ni and S.-H. Yu, A Flexible and Highly Pressure-Sensitive Graphene–Polyurethane Sponge Based on Fractured Microstructure Design, *Adv. Mater.*, 2013, **25**(46), 6692–6698.
16 Z. Chen, W. Ren, L. Gao, B. Liu, S. Pei and H.-M. Cheng, Three-dimensional flexible and conductive interconnected graphene networks grown by chemical vapour deposition, *Nat. Mater.*, 2011, **10**(6), 424–428.
17 V. Eswaraiah, V. Sankaranarayanan and S. Ramaprabhu, Functionalized Graphene–PVDF Foam Composites for EMI Shielding, *Macromol. Mater. Eng.*, 2011, **296**(10), 894–898.
18 Y. A. Samad, Y. Li, S. M. Alhassan and K. Liao, Novel Graphene Foam Composite with Adjustable Sensitivity for Sensor Applications, *ACS Appl. Mater. Interfaces*, 2015, **7**(17), 9195–9202.
19 Y. A. Samad, Y. Li, A. Schiffer, S. M. Alhassan and K. Liao, Graphene Foam Developed with a Novel Two-Step Technique for Low and High Strains and Pressure-Sensing Applications, *Small*, 2015, **11**(20), 2380–2385.
20 Y. Hernandez, V. Nicolosi, M. Lotya, F. M. Blighe, Z. Sun, S. De, I. T. McGovern, B. Holland, M. Byrne, Y. K. Gun'Ko, J. J. Boland, P. Niraj, G. Duesberg, S. Krishnamurthy, R. Goodhue, J. Hutchison, V. Scardaci, A. C. Ferrari and J. N. Coleman, High-yield production of graphene by liquid-phase exfoliation of graphite, *Nat. Nanotechnol.*, 2008, **3**(9), 563–568.
21 J. N. Coleman, M. Lotya, A. O'Neill, S. D. Bergin, P. J. King, U. Khan, K. Young, A. Gaucher, S. De, R. J. Smith, I. V. Shvets, S. K. Arora, G. Stanton, H. Y. Kim, K. Lee, G. T. Kim, G. S. Duesberg, T. Hallam, J. J. Boland, J. J. Wang, J. F. Donegan, J. C. Grunlan, G. Moriarty,

A. Shmeliov, R. J. Nicholls, J. M. Perkins, E. M. Grieveson, K. Theuwissen, D. W. McComb, P. D. Nellist and V. Nicolosi, Two-dimensional nanosheets produced by liquid exfoliation of layered materials, *Science*, 2011, **331**(6017), 568–571.

22 M. Lotya, Y. Hernandez, P. J. King, R. J. Smith, V. Nicolosi, L. S. Karlsson, F. M. Blighe, S. De, Z. Wang, I. T. McGovern, G. S. Duesberg and J. N. Coleman, Liquid Phase Production of Graphene by Exfoliation of Graphite in Surfactant/Water Solutions, *J. Am. Chem. Soc.*, 2009, **131**(10), 3611–3620.

23 M. Lotya, P. J. King, U. Khan, S. De and J. N. Coleman, High-Concentration, Surfactant-Stabilized Graphene Dispersions, *ACS Nano*, 2010, **4**(6), 3155–3162.

24 K. R. Paton, E. Varrla, C. Backes, R. J. Smith, U. Khan, A. O'Neill, C. Boland, M. Lotya, O. M. Istrate, P. King, T. Higgins, S. Barwich, P. May, P. Puczkarski, I. Ahmed, M. Moebius, H. Pettersson, E. Long, J. Coelho, S. E. O'Brien, E. K. McGuire, B. M. Sanchez, G. S. Duesberg, N. McEvoy, T. J. Pennycook, C. Downing, A. Crossley, V. Nicolosi and J. N. Coleman, Scalable production of large quantities of defect-free few-layer graphene by shear exfoliation in liquids, *Nat. Mater.*, 2014, **13**(6), 624–630.

25 P. May, U. Khan, J. M. Hughes and J. N. Coleman, Role of Solubility Parameters in Understanding the Steric Stabilization of Exfoliated Two-Dimensional Nanosheets by Adsorbed Polymers, *J. Phys. Chem. C*, 2012, **116**(20), 11393–11400.

26 J. N. Coleman, Liquid-Phase Exfoliation of Nanotubes and Graphene, *Adv. Funct. Mater.*, 2009, **19**(23), 3680–3695.

27 J. N. Coleman, Liquid exfoliation of defect-free graphene, *Acc. Chem. Res.*, 2013, **46**(1), 14–22.

28 C. S. Boland, S. Barwich, U. Khan and J. N. Coleman, High stiffness nano-composite fibres from polyvinylalcohol filled with graphene and boron nitride, *Carbon*, 2016, **99**, 280–288.

29 J. Du and H.-M. Cheng, The Fabrication, Properties, and Uses of Graphene/Polymer Composites, *Macromol. Chem. Phys.*, 2012, **213**(10–11), 1060–1077.

30 U. Khan, P. May, A. O'Neill and J. N. Coleman, Development of stiff, strong, yet tough composites by the addition of solvent exfoliated graphene to polyurethane, *Carbon*, 2010, **48**(14), 4035–4041.

31 H. Kim, A. A. Abdala and C. W. Macosko, Graphene/Polymer Nanocomposites, *Macromolecules*, 2010, **43**(16), 6515–6530.

32 T. Kuilla, S. Bhadra, D. Yao, N. H. Kim, S. Bose and J. H. Lee, Recent advances in graphene based polymer composites, *Prog. Polym. Sci.*, 2010, **35**(11), 1350–1375.

33 P. May, U. Khan, A. O'Neill and J. N. Coleman, Approaching the theoretical limit for reinforcing polymers with graphene, *J. Mater. Chem.*, 2011, **22**(4), 1278–1282.

34 J. R. Potts, D. R. Dreyer, C. W. Bielawski and R. S. Ruoff, Graphene-based polymer nanocomposites, *Polymer*, 2011, **52**(1), 5–25.

35 S. Stankovich, D. A. Dikin, G. H. B. Dommett, K. M. Kohlhaas, E. J. Zimney, E. A. Stach, R. D. Piner, S. T. Nguyen and R. S. Ruoff, Graphene-based composite materials, *Nature*, 2006, **442**(7100), 282–286.

36 R. J. Young, I. A. Kinloch, L. Gong and K. S. Novoselov, The mechanics of graphene nanocomposites: A review, *Compos. Sci. Technol.*, 2012, **72**(12), 1459–1476.

37 U. Khan, P. May, A. O'Neill, J. J. Vilatela, A. H. Windle and J. N. Coleman, Tuning the Mechanical Properties of Composites from Elastomeric to Rigid Thermoplastic by Controlled Addition of Carbon Nanotubes, *Small*, 2011, **7**(11), 1579–1586.

38 U. Khan, P. May, A. O'Neill, A. P. Bell, E. Boussac, A. Martin, J. Semple and J. N. Coleman, Polymer reinforcement using liquid-exfoliated boron nitride nanosheets, *Nanoscale*, 2013, **5**(2), 581–587.

39 U. Khan, P. May, H. Porwal, K. Nawaz and J. N. Coleman, Improved Adhesive Strength and Toughness of Polyvinyl Acetate Glue on Addition of Small Quantities of Graphene, *ACS Appl. Mater. Interfaces*, 2013, **5**(4), 1423–1428.

40 S. Xie, O. M. Istrate, P. May, S. Barwich, A. P. Bell, U. Khan and J. N. Coleman, Boron nitride nanosheets as barrier enhancing fillers in melt processed composites, *Nanoscale*, 2015, **7**(10), 4443–4450.

41 U. Khan, A. O'Neill, M. Lotya, S. De and J. N. Coleman, High-Concentration Solvent Exfoliation of Graphene, *Small*, 2010, **6**(7), 864–871.

42 M. Sahini, *Applications of Percolation Theory*, CRC Press, 1994.

43 D. S. Mclachlan, M. Blaszkiewicz and R. E. Newnham, Electrical-Resistivity of Composites, *J. Am. Ceram. Soc.*, 1990, **73**(8), 2187–2203.